



Orthopyroxene oikocrysts in the MG1 chromitite layer of the Bushveld Complex: implications for cumulate formation and recrystallisation

Felix E. D. Kaufmann^{1,2} · Zoja Vukmanovic³ · Marian B. Holness³ · Lutz Hecht^{1,2}

Received: 15 August 2017 / Accepted: 18 January 2018 / Published online: 30 January 2018
© Springer-Verlag GmbH Germany, part of Springer Nature 2018

Abstract

Two typical mineral textures of the MG 1 chromitite of the Bushveld Complex, South Africa, were observed; one characterised by abundant orthopyroxene oikocrysts, and the other by coarse-grained granular chromitite with only minor amounts of interstitial material. Oikocrysts form elongate clusters of several crystals aligned parallel to the layering, and typically have subhedral, almost chromite-free, core zones containing remnants of olivine. The core zones are surrounded by poikilitic aureoles overgrowing euhedral to subhedral chromite chadacrysts. Chromite grains show no preferred crystal orientation, whereas orthopyroxene grains forming clusters commonly share the same crystallographic orientation. Oikocryst core zones have lower Mg# and higher concentrations of incompatible trace elements compared to their poikilitic aureoles. Core zones are relatively enriched in REE compared to a postulated parental magma (B1) and did not crystallise in equilibrium with the surrounding minerals, whereas the composition of the poikilitic orthopyroxene is consistent with growth from the B1 magma. These observations cannot be explained by the classic cumulus and post-cumulus models of oikocryst formation. Instead, we suggest that the oikocryst core zones in the MG1 chromitite layer formed by peritectic replacement of olivine primocrysts by reaction with an upwards-percolating melt enriched in incompatible trace elements. Poikilitic overgrowth on oikocryst core zones occurred in equilibrium with a basaltic melt of B1 composition near the magma-crystal mush interface. Finally, adcumulus crystallisation followed by grain growth resulted in the surrounding granular chromitite.

Keywords Oikocryst · Bushveld Complex · Layered intrusions · Cumulate formation · Subsolvus processes

Introduction

Despite the long history of research and the wealth of scientific publications, the mechanisms by which layering forms in mafic intrusions are not well understood. Due to their ubiquity in cumulate rocks and their ability to preserve different stages of the solidification process, the microstructural and geochemical study of oikocrysts can contribute to our

understanding of layering mechanisms (Namur et al. 2015, and references therein).

Oikocrysts are large crystals that enclose smaller crystals (chadacrysts) to form a poikilitic texture. Many different minerals form oikocrysts, such as pyroxene (e.g., this study; Cameron 1969, 1975; Ulmer and Gold 1982; Campbell 1987; Mathison 1987; Barnes et al. 2016), plagioclase (e.g., Cameron 1969) olivine (e.g., Maier 1995; O'Driscoll et al. 2009) and hornblende (e.g., Meurer and Claeson 2002; Ivanic et al. 2015). The formation of poikilitic textures are dependent on differences in the nucleation rate (Wager 1961) and/or the growth rate (Vernon 2004, p. 106) of the different minerals: oikocrysts form if one mineral has a lower nucleation rate but higher growth rate than co-accumulating crystals of another phase.

There are two main hypotheses to explain the formation of oikocrysts. Early work was based on the hypothesis that oikocrysts form in the post-cumulus stage by the solidification of interstitial liquid (Wager et al. 1960), whereas recent studies argue that the absence of compositional zonation and

Communicated by Chris Ballhaus.

✉ Felix E. D. Kaufmann
felix.kaufmann@mfn-berlin.de

¹ Museum für Naturkunde Berlin, Leibnitz-Institut für Evolutions- und Biodiversitätsforschung, Invalidenstrasse 43, 10115 Berlin, Germany

² Institut für Geologische Wissenschaften, Freie Universität Berlin, Malteserstr. 74-100, 12449 Berlin, Germany

³ Department of Earth Sciences, University of Cambridge, Downing Street, Cambridge CB2 3EQ, UK

the similarity of composition of the oikocrysts and nearby primocrysts of the same phase point to the oikocrysts being cumulus grains (Campbell 1968; Mathison 1987; Tegner and Wilson 1995; Barnes et al. 2016).

In this study, we report the results of an investigation of oikocrysts in a chromitite layer of the Rustenburg Layered Suite of the Bushveld Intrusion, South Africa. Our approach integrates the microstructural and geochemical evolution of the orthopyroxene oikocrysts, using electron back-scatter diffraction (EBSD), electron microprobe analysis (EMP) and LA-ICP-MS. These different analytical approaches lead to a model by which we explain the formation of orthopyroxene oikocrysts by reactive replacement of olivine primocrysts by an upwards-percolating melt, followed by poikilitic overgrowth of oikocryst cores from a more primitive melt. Post-cumulus growth and textural modification resulted in the observed composition and microstructure of the granular chromitite.

Geological setting

The Bushveld Complex, located in the NE of South Africa (Fig. 1) is the largest known plutonic complex on Earth, hosting the world's greatest reserves of platinum-group

elements, chromium and vanadium. It is of Proterozoic age (Scoates and Friedman 2008; Scoates and Wall 2015), and intruded into sedimentary rocks of the Transvaal Supergroup. It covers an area of over 65,000 km² and ranges in thickness from 7 to 9 km (Eales and Cawthorn 1996; Cawthorn 2015). According to the South African Committee for Stratigraphy (1980), the complex is divided into the ultramafic–mafic Rustenburg Layered Suite and the felsic Lebowa Granite and Rashedoop Granophyre. The Rustenburg Layered Suite has a saucer-like shape dipping gently towards the centre of the complex.

The compositions of the parental magmas of the Rustenburg Layered Suite have been estimated from fine-grained sills and chilled margins (Harmer and Sharpe 1985; Barnes et al. 2010; Godel et al. 2011; Wilson 2012). Three different parental magmas have been proposed: an Mg-rich basaltic andesite known as B1, and tholeiitic basalts known as B2 and B3. The suite is subdivided from bottom to top into the lower zone, critical zone, main zone and upper zone. The B1 magma is suggested to have formed the lower zone and lower critical zone.

Chromitite layers occur throughout the critical zone. They are subdivided into the lower (LG), middle (MG) and upper (UG) groups. Each group is numbered from bottom to top; thus the MG1 layer is the first chromitite of the Middle

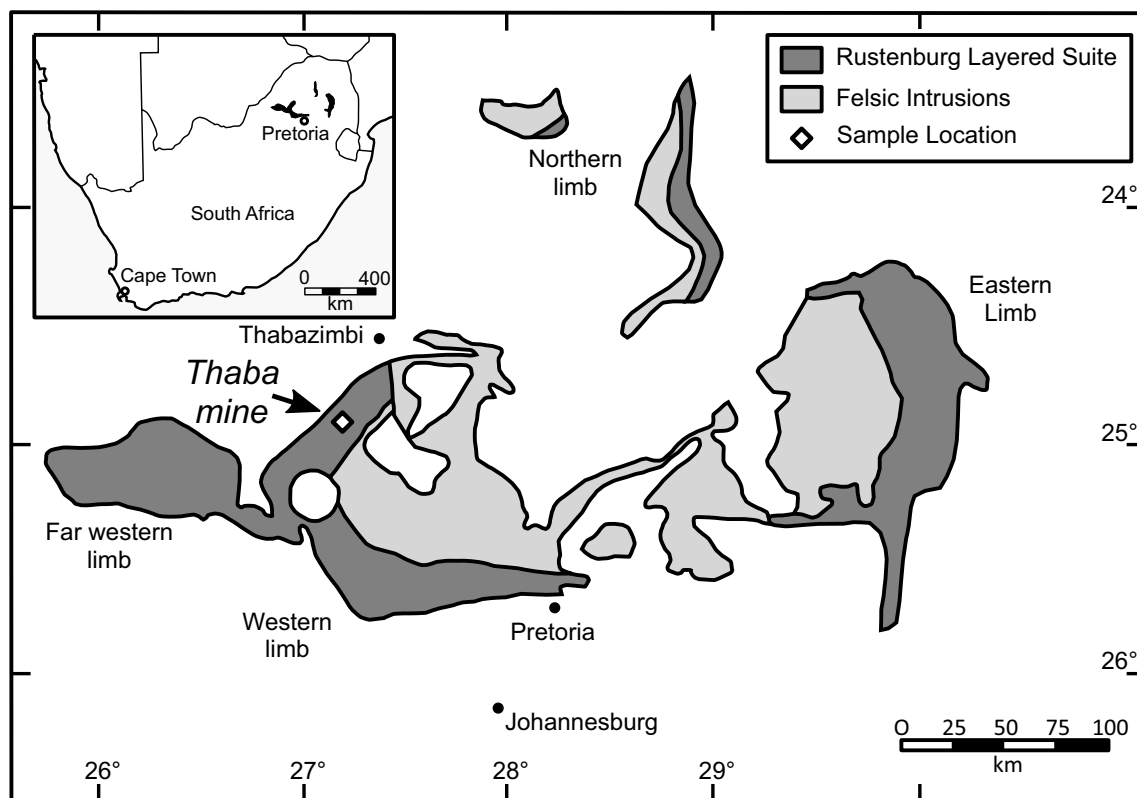


Fig. 1 Schematic geological map of the Bushveld Complex with sample location (after Eales and Cawthorn 1996)

Group. Chromitites vary in thickness from ~ 1 m to small stringers only cm to mm thick. Chromitites may contain pyroxenitic layers, known as partings.

Scientific publications on chromitite layers in the Rustenburg Layered Suite are mainly focussed on the UG2 chromitite, which is the richest in platinum-group elements. However, the MG layers have also been the subject of many published studies (e.g., Cameron 1969, 1977, 1980; Lee and Parry 1988; Eales et al. 1990; Teigler 1990; Merkle 1992; Scoon and Teigler 1994; Kottke-Levin et al. 2009; Naldrett et al. 2009; Junge et al. 2016; Oberthuer et al. 2016). Published studies of mineral chemistry (Cameron 1977, 1980; Eales et al. 1990; Kottke-Levin et al. 2009) concentrated on the broader successions of the LG and MG chromitites and their adjacent host rocks, proposing a range of different mechanisms of chromitite genesis such as externally controlled changes in confining pressure (Cameron 1977, 1980), and reaction of the resident magma with influxes of primitive magma (Eales et al. 1990). Cameron (1969) focused on possible post-cumulus changes in chromitite layers, providing a textural description of orthopyroxene oikocrysts similar to those investigated in this study. More detailed investigations have been conducted on the platinum-group element and platinum-group mineral concentration and distribution (Lee and Parry 1988; Teigler 1990; Merkle 1992; Scoon and Teigler 1994; Junge et al. 2016; Oberthuer et al. 2016).

Sample material and analytical methods

Sample material comes from drill core ZK135 from the Thaba open pit mine (Fig. 1), which covers the LG6 to MG2 chromitite layers and their host rocks. Core material was provided by Cronimet Chrome Mining SA (Pty) Ltd. In this section of stratigraphy, the MG1 chromitite is 62 cm thick, embedded in pyroxenite with an intermediate ca. 15 cm thick pyroxenite–chromitite transition zone (Fig. 2a). This study focuses on the cm-sized orthopyroxene oikocrysts that occur in the lower and upper part of the MG1 chromitite layer (Fig. 2b, c).

For textural characterisation, the central chadacryst-free regions of 45 oikocrysts were outlined on thin section scans, and the program ImageJ was used to measure major and minor axis length, size, orientation, and spatial distribution. We term this region the oikocryst ‘core zone’, defined as the central chadacryst-free area that is surrounded by orthopyroxene containing abundant small idiomorphic chromite grains, which varies from 1.3 to 6.2 mm across. The core zone can comprise several subgrains with different crystallographic orientations, which were treated separately for the alignment analysis. The extent of any preferred alignment of non-equant oikocryst core zones was calculated using the program CSDCorrections 1.53

by Higgins (2000) (see Meurer and Boudreau (1998b) and Boorman et al. (2004) for further information), which provides the alignment factor: this ranges from 0 (no statistically significant alignment) to 100 (perfect alignment of grains). Crystal size distributions (CSD) were measured both for chromite grains enclosed in the poikilitic pyroxenite and for chromite in granular chromitite. For this, we used compiled backscattered electron (BSE) images and the program CSDCorrections 1.53 following the methods of Higgins (2000). The following input parameters were used for the calculation of the CSD histograms: maximum grain diameter (minimum diameter of chromite grains was set to 0.01 mm), a massive fabric, chromite shape of 1:1:1 and a roundness of 0.2.

After standard mechanical polishing using diamond paste, thin sections were polished for 1 h with 0.06 µm colloidal silica (SiO₂ particle dispersion in an alkaline solution) at the University of Cambridge, UK. Samples were analysed on a FEI sFEG XL30 SEM at the Department of Physics, University of Cambridge. All crystallographic datasets were collected, indexed and analysed using Oxford Instruments AZtec acquisition software, set to detect 6 bands, 60 Hough transforms, 75 reflectors, and at 4 × 4 binning. Whole thin section EBSD was carried out using 15 µm step size. EBSD maps and pole figures of crystallographic orientation were constructed using Oxford Instrument Channel 5 software. Inverse pole figure maps represent the orientation of the crystal lattice along specific directions of the sample reference frame (Y–X). Crystallographic orientation data (pole figures and inverse pole figures) were plotted using Channel 5 “Mambo” software using lower hemisphere, equal area projections. Data are reported with respect to an arbitrarily assigned X–Y reference frame. Chromite density contour diagrams are calculated on point per grain pole figures, using half width of 20° and cluster size of 10°.

EMP analyses were carried out at the Museum für Naturkunde Berlin with a JEOL JXA-8500F EMP equipped with a field emission cathode and five wavelength-dispersive spectrometers. The following analytical conditions were used: 20 kV accelerating voltage for chromite and 15 kV for pyroxene measurements, 75 and 15 nA beam current for chromite and pyroxene, respectively. The spot size was set to 1 µm for chromite and 2 µm for pyroxene. The measured intensities were calibrated against natural minerals of the Smithsonian international standard suite (Jarosewich et al. 1980) and pure metals of the Astimex metal standard. Matrix effects were minimised by a conventional ZAF routine processed by the JEOL series operating system. Accuracy and reproducibility were checked regularly before and after each analysis session by measurements of minerals of the Smithsonian mineral standards (Chromite, USNM 117075; Augite, USNM 122142; Hypersthene USNM 746, Jarosewich et al. 1980), which revealed deviations of < 2%. The

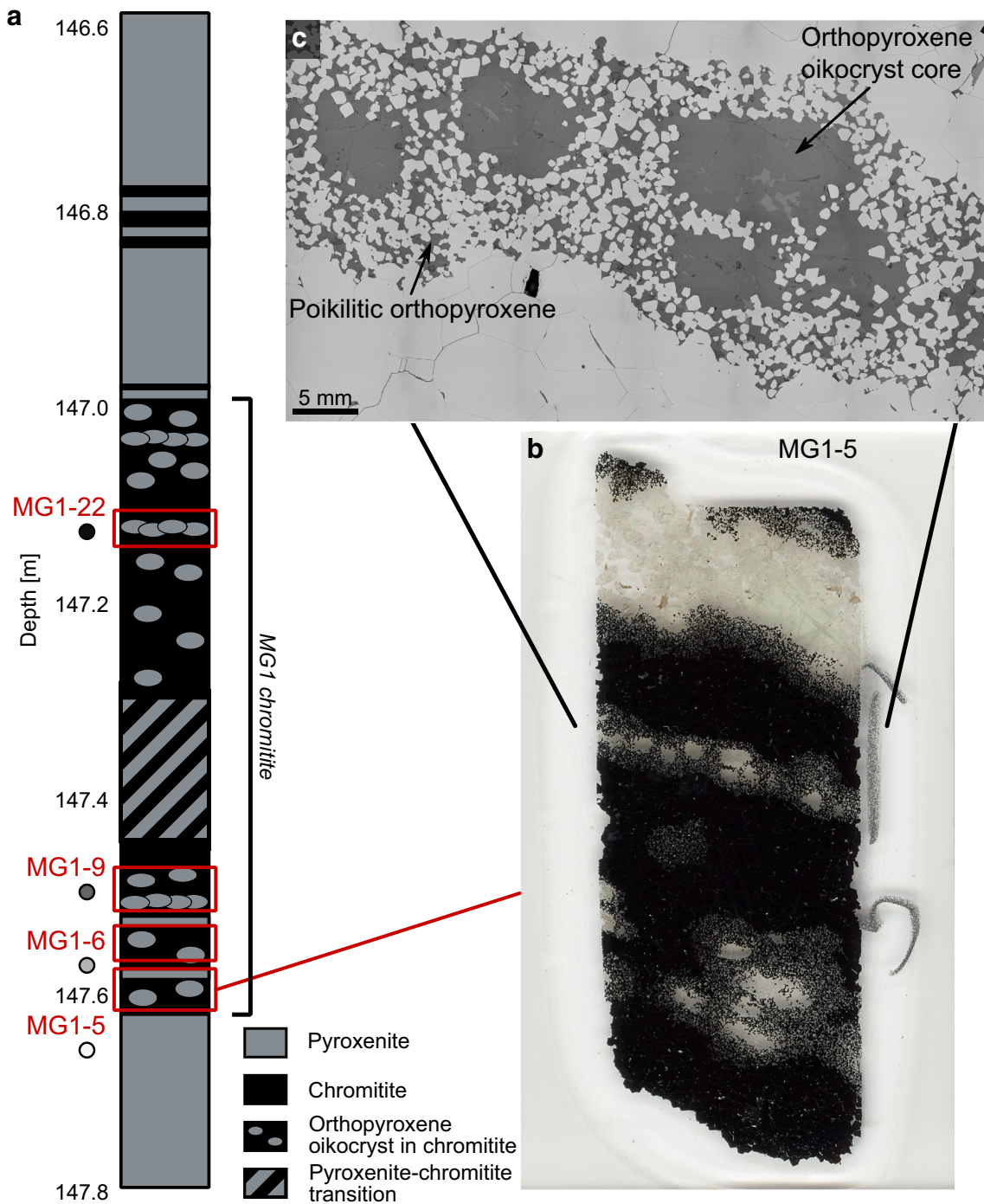


Fig. 2 a Lithostratigraphic column of the MG1 chromitite layer with investigated areas (red boxes) and marker colour used in the following figures. b Photograph of petrographic thin section with typical

appearance of orthopyroxene oikocrysts. c Composed backscattered electron image of oikocrysts forming a layer parallel to the overall layering

ferric iron content of chromite and pyroxene was calculated assuming ideal stoichiometry.

LA-ICP-MS analyses for trace element concentrations in orthopyroxene were conducted at the Institut für Mineralogie of the Leibniz Universität Hannover (LUH) with a

fast scanning-sector field-ICP-MS (ThermoScientific ElementXR) connected to a femtosecond (Ti-sapphire) laser ablation system. Details of the fs-LA system are given in Oeser et al. (2014) and Lazarov and Horn (2015). In our study, the laser operated at 20–30 Hz, with a spot size

ranging between 40 and 50 μm in diameter. The ablation mode was set to raster mode for analyses in the oikocryst cores and to line mode for analyses at the rims and in poikilitic orthopyroxene. Acquisition times of the background signal and the ablation signal were set to 40 and 100 s, respectively. Sample surfaces of each spot were pre-ablated before measurement to avoid artefacts due to surface contamination. Analyses were bracketed every 10–15 measurements by standard reference material NIST610 to correct for internal instrumental drift. Si concentrations, obtained by EMP analyses, were used for the internal calibration of trace element concentration for orthopyroxene. Further testing of the accuracy and reproducibility was undertaken by measuring silicate reference material (BCR-2G), indicating accuracy and reproducibility of 1–5%. Further information about trace element analyses by fs-LA-ICP-MS at the LUH is given in Albrecht et al. (2014) and Collinet et al. (2017). Data processing was performed with the SILLS program (Guillong et al. 2008).

Results

Petrography

The MG 1 chromitite layer comprises granular chromitite, with only minor amounts of interstitial material, surrounding large isolated orthopyroxene oikocrysts characterised by an inclusion-free core zone that is typically ovoid. The proportion of chromite decreases from the uppermost part of the chromitite into the hanging wall, which is formed of cumulus orthopyroxene, 1–10 vol% chromite, and minor amounts of interstitial plagioclase and clinopyroxene. The chromitite layer contains three mm-thick pyroxenitic partings parallel to the overall layering, while four additional mm-thick chromitite layers are embedded in the hanging wall pyroxenite. The footwall of the MG1 is a feldspathic pyroxenite, and is separated from the overlying main chromitite layer by a heavily altered coarse-grained chromite-rich (10–25 vol%) pyroxenite with remnants of olivine overgrown by orthopyroxene.

The poikilitic aureoles surrounding the inclusion-free core zones contain 50–60 vol% euhedral to subhedral chromite grains. Although most oikocrysts have chadacryst-free core zones, some do not: we ascribe this to a 2D cut effect. Oikocrysts are either isolated or form clusters of several crystals elongated parallel to the layering (Fig. 3a). The grain boundaries between different crystals of orthopyroxene do not always correspond to the apparent margins of the oikocrysts. Importantly, the orthopyroxene in adjacent oikocrysts is commonly in optical continuity, and the grain boundaries between adjacent crystals may pass through an oikocryst (Fig. 3c). Oikocryst core zones are not always

entirely inclusion-free, but may contain small grains of chromite, olivine, clinopyroxene and, rarely, biotite and hornblende. The olivine inclusions are commonly lobate, with a shape entirely unlike that expected for primocrysts (Fig. 3b). Some exsolution lamellae of clinopyroxene are present (Fig. 3b, e). Hydrous silicate inclusions follow the orthopyroxene cleavage and are restricted to the lower part of the MG1.

Chromite grains show a wide range of grain sizes: the few grains in the oikocryst core zones are 0.02–0.15 mm across, in contrast to those in the outer poikilitic aureoles which are 0.06–0.3 mm, whereas the massive chromitite grains are 0.4–1.1 mm across. Chadacrysts generally increase in size outwards from the oikocryst core (Fig. 3d). The chromitite hosting the oikocryst has a granular texture (Fig. 3f) with <5 vol% interstitial material, which is mainly biotite, hornblende and serpentine. Minor amounts of apatite and sulphides are present. Chromite in granular chromitite has 120° triple junctions and smoothly curved grain boundaries. Plagioclase is absent throughout the chromitite seam (upper and lower part) but is present in the chromitite-pyroxenite transition, which comprises cumulus orthopyroxene with interstitial plagioclase and hornblende (Fig. 3g). The pyroxenite immediately underlying the chromitite has similar microstructural characteristics to the oikocrystic layers in the chromitite: the chromite framework is overgrown by coarse-grained orthopyroxene enclosing olivine in the former cores.

Microstructural analysis

The average aspect ratio of oikocryst cores is 1.80 (± 0.51 SD), and they display a systematic alignment (Fig. 2b), with an alignment factor of 73 (on the basis of 45 grains). By comparison with Meurer and Boudreau (1998b), the uncertainty on this value is likely to be in the range ± 2 –3. The general dip of the shape preferred orientation of the oikocryst core zones is parallel to the overall layering ($15^\circ \pm 22^\circ$ SD from the horizontal borehole).

Independent of their size, chromite crystals, either those enclosed by oikocrysts or those outside oikocrysts, show no overall crystallographic preferred orientation (CPO, Fig. 4). However, small groups or clusters of grains in both the coarse-grained band and where enclosed by orthopyroxene oikocrysts occasionally show similar crystallographic orientations along a particular sample direction (examples are outlined with white lines in Fig. 4a). Most of these clusters with similar crystallographic orientations do not contain more than 4–5 grains per cluster (as viewed in thin section). While each cluster contains at least one common axis along the x-direction of the sample reference frame (e.g., $\langle 110 \rangle$ in the case of cluster 2 shown in Fig. 4d), one cluster shown in Fig. 4d (labelled cluster 1) shares the common axis $\langle 001 \rangle$ in all three sample directions (Fig. 4d). The axis

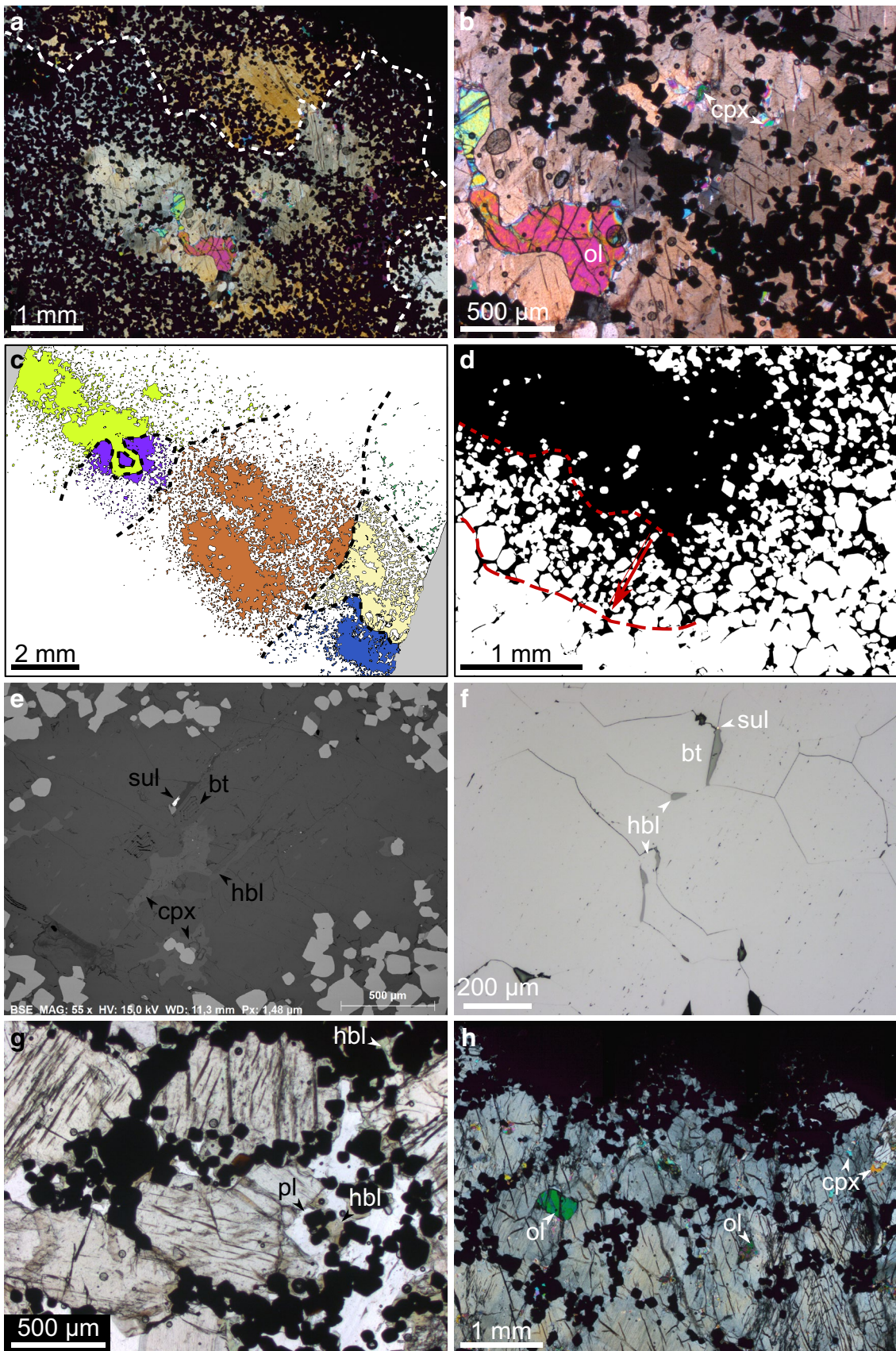


Fig. 3 Photomicrographs in crossed polarised light. Note that the thin sections are ~ 100 μm thick and therefore minerals show birefringence colours of higher than usual order. **a** Overview of oikocryst cluster consisting of three different orthopyroxene crystals. Grain boundaries of orthopyroxene with same crystallographic orientation are illustrated by dashed lines. **b** Olivine (ol) and clinopyroxene (cpx) inclusions in orthopyroxene oikocryst core zone. **c** Sketch of oikocryst layer, showing the complex relationships between orthopyroxene crystals (each coloured differently). **d** Sketch of poikilitic aureole. The arrow indicates the increase in grain size for chromite from the core zone (upper part) to the granular chromitite (lower part). **e** Backscattered electron image of oikocryst cores with sulphide (sul), biotite, hornblende and clinopyroxene inclusions. Note that hydrous silicates are oriented parallel to the cleavage of the orthopyroxene. **f** Reflected light photomicrographs of granular chromitite. Chromite shows 120° triple junctions and smooth curved grain boundaries. Interstitial phases consist mainly of hornblende (hbl) and biotite (bt). **g** Chromitite–pyroxenite transition in plain polarised light with cumulus orthopyroxene and interstitial plagioclase (pl) and hornblende. **h** Footwall pyroxenite consisting of pegmatoidal orthopyroxene overgrowing the chromite framework

that most commonly occurs as a common direction relating the individual grains within a cluster is $\langle 100 \rangle$, with $\langle 110 \rangle$ and $\langle 111 \rangle$ being progressively less common (Fig. 4). The inverse pole figure map for orthopyroxene reveals large areas with a single crystallographic orientation (Fig. 5a, b). Sample MG1–22 contains two adjacent oikocrysts whose (001) planes are offset by only a few degrees (Fig. 5c). Large orthopyroxene oikocrysts from MG1–5 are almost all in optical continuity (Fig. 5d).

CSD plots for chromite enclosed in poikilitic orthopyroxene (Fig. 6a) and chromite in granular chromitite (Fig. 6b) are both straight. However, that for granular chromite is rotated towards larger grains with a shallower slope compared to that for chromite enclosed by the oikocrysts.

Orthopyroxene and olivine composition

There are clear differences in the composition of orthopyroxene oikocryst core zones compared to the surrounding poikilitic aureoles (Table 1). Oikocryst core zones have lower Mg# [atomic ratio, $\text{Mg}/(\text{Mg} + \text{Fe}^{2+})$] and higher concentrations of minor (CaO , Al_2O_3) and trace elements (Zr) compared to poikilitic orthopyroxene (Fig. 7). Only TiO_2 concentrations display an opposing trend towards higher concentrations in poikilitic orthopyroxene (Fig. 7d). The composition of the orthopyroxene forming the outermost ~ 100 μm of the core zones is intermediate between that of the centre of the core zones and that of the poikilitic aureoles. Ce/Yb ratios (Fig. 7f) reveal a similar behaviour for the REE concentrations in the poikilitic aureole and in the central and outermost part of the core zone, with the highest concentrations for light and heavy REE in the central part of the core zones. Orthopyroxene chemistry displays a decrease in trace element concentrations

towards the top of the MG1 layer [light grey via medium grey towards black tone (e.g., Fig. 7f)]. Our data are in good agreement with other studies of orthopyroxene chemistry in the chromitite layers of the Bushveld Complex (e.g., Eales et al. 1993; Veksler et al. 2015).

For comparison we calculated the REE composition of orthopyroxene that would have crystallised from a postulated parental B1 magma, using the B1 composition of Barnes et al. (2010) and partition coefficients for orthopyroxene from Sun and Liang (2013) and Yao et al. (2012) for 750° and 1250 °C. The observed REE concentrations are notably higher in core zones compared to those expected from our calculations (Fig. 7f).

Similar trends can be observed in the REE signatures. Our results, normalised relative to the B1 magma, are shown in Fig. 8. In general, all measurements show a shift towards lower REE concentrations along the MG1 chromitite seam from bottom to top. Core zone, outer core zone and poikilitic aureole REE concentrations are clearly different. Poikilitic orthopyroxene has lower concentrations compared to oikocryst core zones, with intermediate compositions in the outer part of the core zones. Furthermore, the general slope of core zone and poikilitic aureole REE patterns vary: poikilitic orthopyroxene has a much steeper slope towards the light REE, as demonstrated by average Ce/Tb ratios of 12.327 in oikocryst core zones compared with ratios of 3.542 in poikilitic orthopyroxene for sample MG1–5 (Table 1). All patterns reveal a negative Eu anomaly, although this is less pronounced in the poikilitic aureoles.

The oikocryst core zones are clearly enriched in REE compared to expected values for orthopyroxene crystallising from B1 magma, regardless of the choice of temperature of crystallisation. Furthermore, the crystallisation temperature controls the slope of the REE pattern, with higher temperatures resulting in a flatter slope (red lines in Fig. 7). The observed composition of the poikilitic aureoles is roughly in agreement with that expected for crystallisation from the B1 magma, although some anomalous enrichment is still observed for the light REE.

The olivine inclusions in the oikocrysts are chemically homogenous. They are enriched in Ni (~ 2800 ppm, Table 2) compared to both the orthopyroxene core zones (~ 570 to 600 ppm) and the poikilitic orthopyroxene aureoles (~ 480 to 530 ppm). They are also enriched in Ni compared with interstitial orthopyroxene (~ 400 ppm) and with cumulus orthopyroxene in the silicate host rocks and pyroxenitic partings in the underlying LG6a and the overlying MG2 chromitite layer (unpublished data). Si and Ni distribution maps (Fig. 9) of the oikocryst core zones reveal no Ni-enrichment surrounding the olivine inclusions.

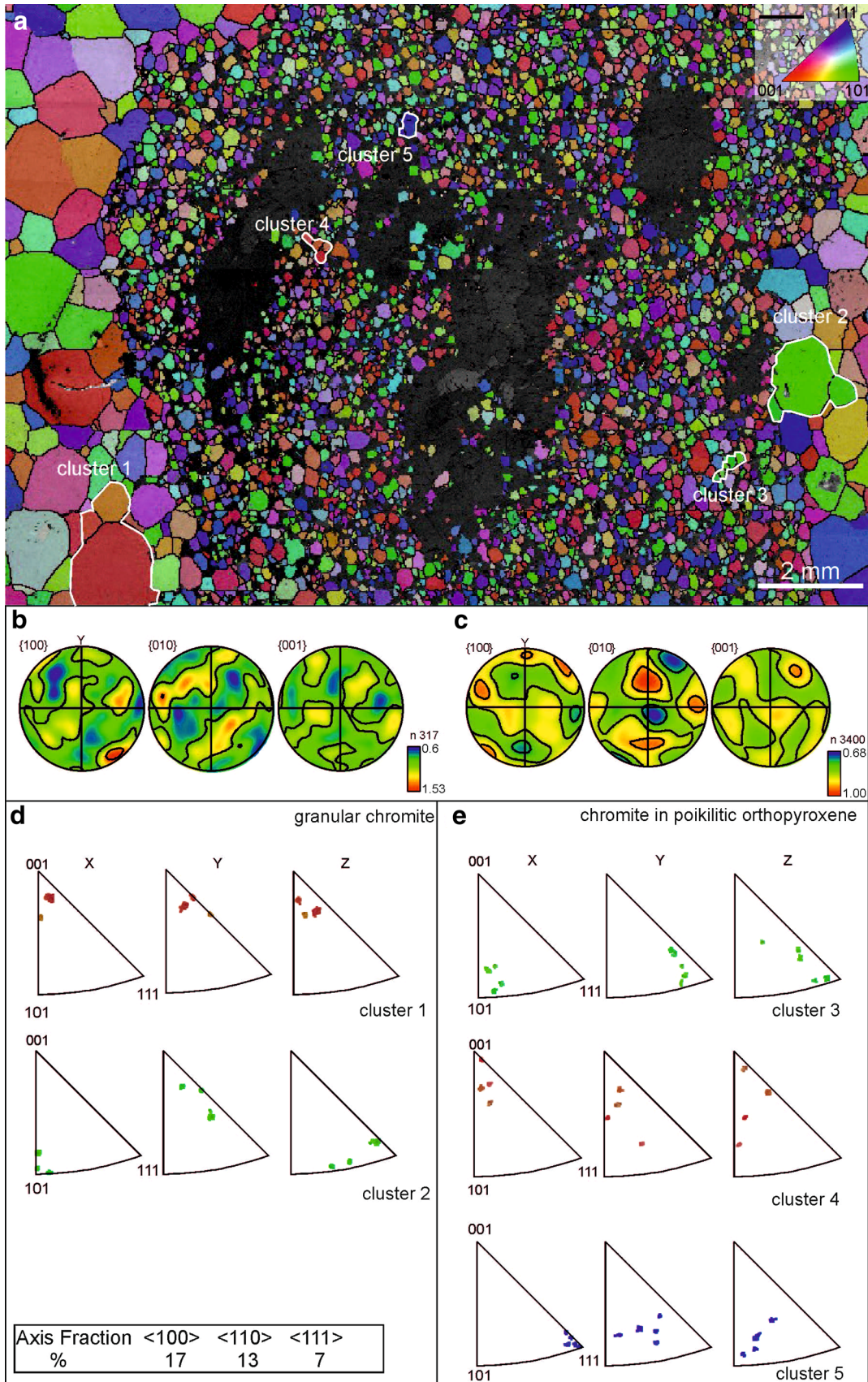


Fig. 4 **a** EBSD inverse pole figure map of chromite grains of the lower part of the MG1, superimposed on a band contrast map. The inverse pole figure map represents the orientation of crystal planes relative to the x-direction of the sample reference frame. The colour scheme is given in the inverse pole figure legend (see inset). White lines outline clusters of chromite crystal with similar crystallographic orientations along the y-direction of the sample reference frame. **b** Density contour diagram (point per grain pole figure) of chromite crystals in poikilitic orthopyroxene. **c** Density contour diagram (point per grain pole figure) of granular chromite calculated with half width of 20° and cluster size of 10°. Both pole figures shown in **b** and **c** are plotted using a lower hemisphere, equal area projection. **d** Inverse pole figure of granular chromite clusters (clusters 1 and 2). **e** Folded inverse pole figure of chromite clusters within the poikilitic orthopyroxene (clusters 3 and 4). Each cluster contains 4 chromite grains. Folded inverse pole figures are plotted using a lower hemisphere, equal area projections. The fraction of the different shared axes is calculated using colour thresholding to identify clusters and presented as an area fraction of all the chromitite grains shown in the EBSD map in **a**

Chromite composition

Chromite shows a clear correlation between texture and chemical composition of both major and trace elements (Table 3). Granular chromite grains have higher Mg# and lower Cr# [Cr/(Cr + Al)] as well as lower TiO₂ concentrations compared to chromite grains enclosed by poikilitic orthopyroxene (Fig. 10a, c). Calculated ferric/ferrous iron ratios reveal slightly higher values in grains enclosed by oikocrysts (Fig. 10b), especially in the upper and lower parts of the MG1 layer. A second minor trend can be observed closer to the middle of the MG1 layer, which contains chromite with almost constant Cr# and Fe³⁺/Fe²⁺ ratios. Remarkably, the upper part of the MG1 is invariably chemically distinct from the lower part.

Discussion

We will now assess the applicability of the two models of oikocryst formation in cumulate rocks, using our textural and chemical observations to evaluate which is most plausible for the orthopyroxene oikocrysts of the Bushveld MG1 chromitite. The critical observations that must be accounted for are:

1. Orthopyroxene oikocrysts contain almost chromite-free core zones, some of which contain olivine remnants, and have poikilitic aureoles containing euhedral to subhedral chromite chadacrysts (Figs. 2, 3d).
2. Oikocrysts occur as either single crystals, or form layer-parallel clusters and groups of several crystals (Figs. 2, 3a, b).
3. The chromitite hosting the oikocryst has a granular texture with only minor amounts of (hydrous) interstitial

material. The microstructure of the chromitite is granular and coarse-grained, with 120° triple junctions and smoothly curved grain boundaries (Figs. 2, 3f, 6).

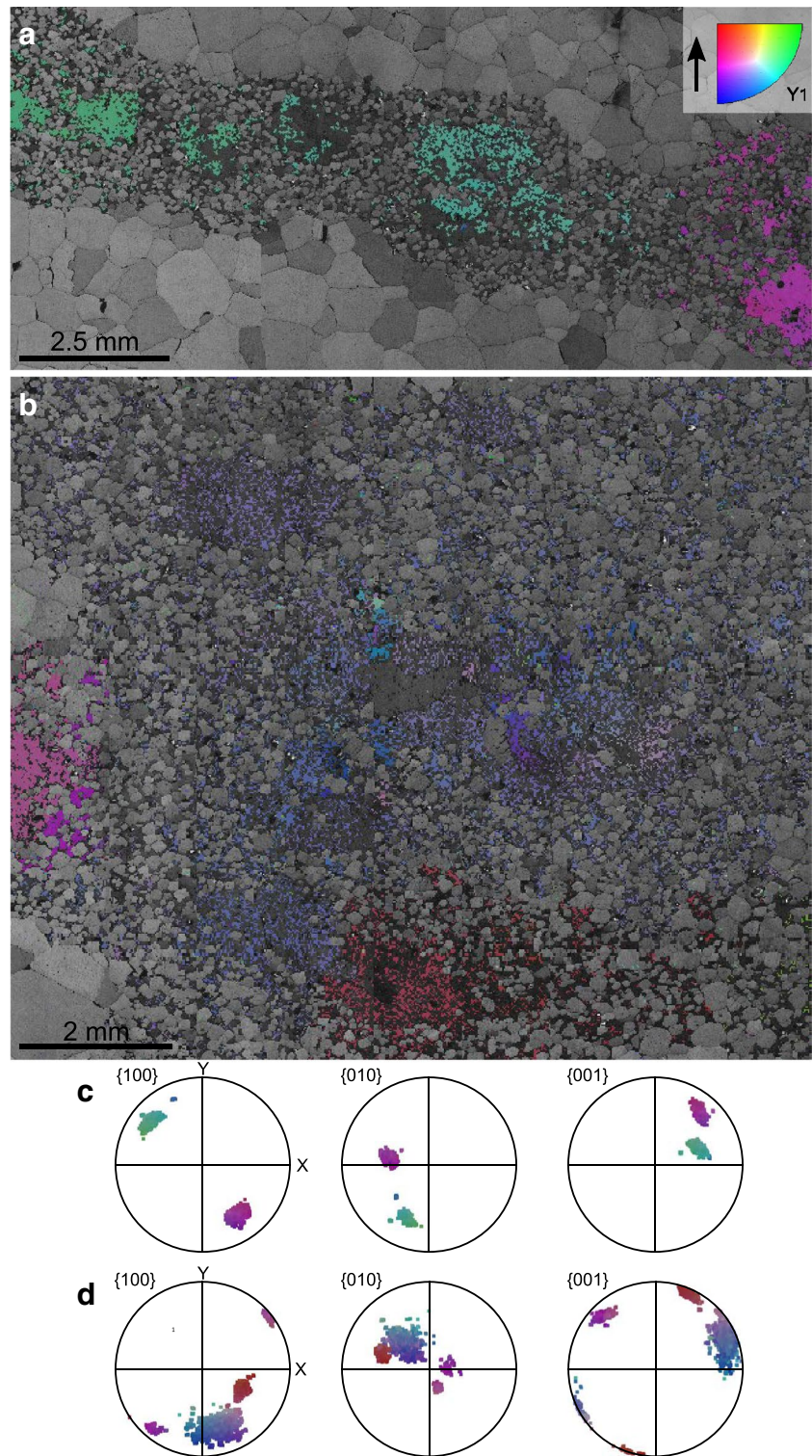
4. Chromite grains show no preferred crystal orientation, neither grains enclosed in poikilitic orthopyroxene nor grains in the granular chromitite, although some form small clusters in which individual grains show some evidence of crystallographic preferred orientations (Fig. 4a).
5. Oikocryst core zones and their poikilitic aureoles have the same crystallographic orientation. Oikocryst aggregates forming clusters and layers are commonly in the same crystallographic orientation (Fig. 5a, b).
6. Mineral chemistry of orthopyroxene core zones and poikilitic aureoles are different: core zones have lower Mg# and higher concentrations in incompatible trace elements, such as Zr and REE, compared to the poikilitic surroundings (Fig. 7).
7. The core zones are enriched in REE compared to the parental magma B1 and could not have crystallised in equilibrium with the surrounding minerals, whereas the composition of the poikilitic aureoles is consistent with growth from such a postulated parental magma (Fig. 8).
8. Granular chromite grains have lower Mg# and lower Cr# compared to chromite grains in poikilitic orthopyroxene (Fig. 10a).

Oikocrysts with partially similar characteristics have been reported from elsewhere in the Rustenburg Layer Suite: in MG1 several km northwards (Veksler, personal communication); the northern part of the Eastern Bushveld (Cameron 1969, 1975); and in the Stillwater Complex where Jackson (1961) described orthopyroxene oikocryst with replaced olivine inclusions in chromitite in great detail. This indicates that our observations may be of general relevance.

Post-cumulus origin of oikocrysts

The first of the post-cumulus models for oikocryst formation was proposed by Wager et al. (1960), who suggested that oikocrysts crystallise from interstitial melt in the cumulus chromite framework. Such an interstitial melt is likely to be relatively evolved and enriched in incompatible elements. Subsidiary re-equilibration of cumulus grains in contact with interstitial melt is thought to result in the post-cumulus enrichment in incompatible elements of cumulus phases, termed the trapped liquid shift effect (TLSE, Barnes 1986; Godel et al. 2011). This cannot explain why the later-crystallising poikilitic orthopyroxene has a composition consistent with growth from a more primitive magma (Fig. 8). Hence, a model involving entirely post-cumulus formation of the orthopyroxene oikocrysts is incompatible with our observations.

Fig. 5 **a, b** EBSD inverse pole figure maps of orthopyroxene grains of the lower part of the MG1, superimposed on a band contrast map. **c** Orthopyroxene pole figure for map **a**. **d** Orthopyroxene pole figure for map **b**. Colour coding of the orthopyroxene pole figures correspond to the inverse pole figure map



Cumulus formation of oikocrysts

The second main hypothesis for oikocryst formation is based on an origin at, or near, the magma-crystal mush interface (e.g., Mathison 1987; Tegner and Wilson 1995; Barnes et al. 2016). Accordingly, oikocrysts either form simultaneously

with cumulus chromite by in situ growth at the magma-crystal mush interface, or form elsewhere and accumulate simultaneously by crystal settling (Hunter 1996; Barnes et al. 2016). These two model variants can be distinguished microstructurally. In situ growth of grains in a gradient of either temperature or composition may lead to a preferred

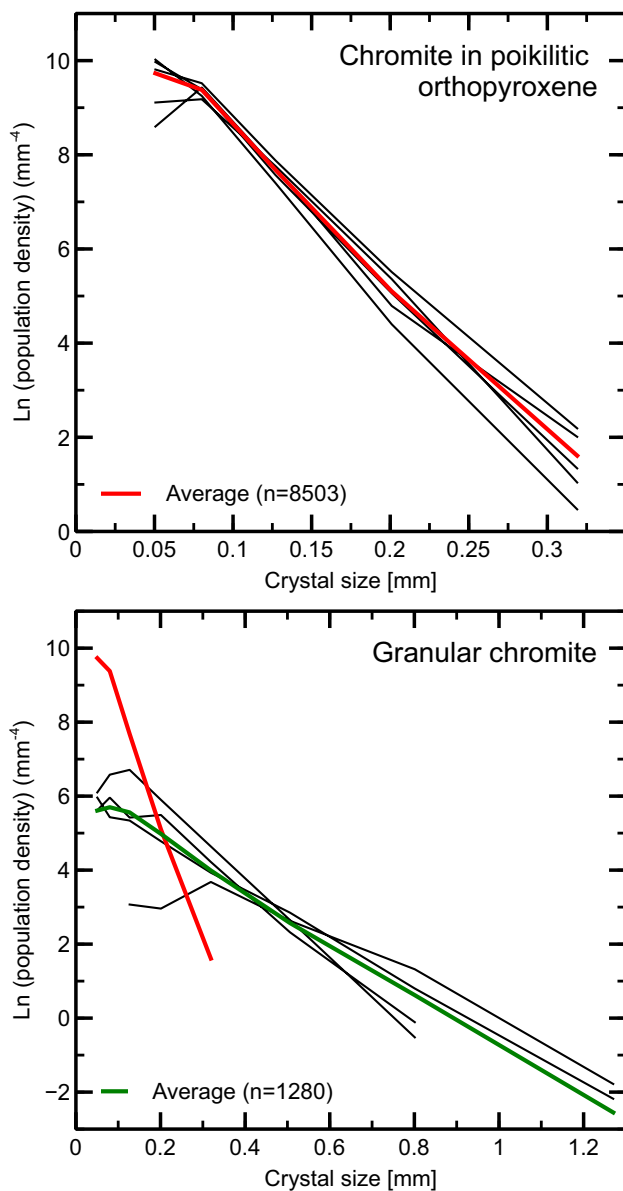


Fig. 6 CSD diagram for **a** chromite enclosed in poikilitic orthopyroxene and **b** for chromite in granular chromitite

orientation of elongate crystals perpendicular to the magma-mush interface (e.g., the harrisites on Rum, Scotland: Wager et al. 1960; O'Driscoll et al. 2007). Conversely, crystal settling, with or without mechanical re-organisation of settled grains by magmatic currents, produces a preferred orientation of elongate grains parallel to the magma-crystal mush interface. Settling or deposition in magmatic currents may also result in grain sorting on the basis of size and/or density. Differing trace element compositions of orthopyroxene oikocryst cores and rims have also been used to argue for a cumulus origin of oikocrysts (Barnes et al. 2016).

Oikocryst core zones in the MG1 chromitite have shapes and orientations characteristic of grains accumulated during

crystal settling (Figs. 2, 3b). Accordingly, the poikilitic orthopyroxene aureoles are therefore overgrowths on cumulus cores (Fig. 3a). The observed compositional differences between core zones and rims could then be explained if the core zones were grown from a different magma to that in which they accumulated. However, this process cannot account for the observation that adjacent oikocrysts have the same crystallographic orientation. Our observations therefore support a two-stage growth history.

Oikocryst formation in the MG1 chromitite: an enhanced model

Our observations support a cumulus origin for the oikocryst core zones, but not as primary orthopyroxene. This is demonstrated by Fig. 3a in which the largest oikocryst core zone, pinched in the middle, contains two resorbed olivine grains, joined by a grain boundary located exactly at the waist of the oikocryst core, consistent with this having originally been two distinct olivine primocrysts. We conclude, therefore, that the core zones are former cumulus olivine crystals that have been replaced by orthopyroxene during peritectic reaction with a relatively Si-rich melt. With the exception of the few remaining remnants of olivine, the replacement was complete, as chemical characteristics of the cumulus olivine (e.g., high Ni concentrations, see Fig. 9; Table 3) are no longer in evidence.

The presence of replacive orthopyroxene oikocrysts only a few cm above the base of the chromitite suggests that original cumulus olivine accumulated shortly after the MG1 layer began to form. While our data cannot be used to specify the process by which chromite accumulated, the aligned layers and clusters of former olivine crystals (Fig. 3a, b) are consistent with the hypothesis that olivine accumulated by crystal settling (Fig. 11a). The likelihood of both olivine and chromite accumulating simultaneously from the same overlying magma source can be assessed by comparing their settling velocities.

A rough estimation of settling velocities in a static liquid can be obtained from Stokes' law, if we assume spherical grains and a low particle concentration:

$$V = \frac{2}{9} \frac{r^2 g (\rho_s - \rho_l)}{\eta},$$

where V is the settling velocity (cm/s), g is gravitational acceleration (981 cm/s^2), r is the radius of a spherical particle (cm), ρ_s is the density of the particle (g/cm^3), ρ_l the density of the liquid (g/cm^3) and η is the viscosity of the (assumed Newtonian) liquid (g/cm s). We used the following values of the parameters to calculate settling velocities for olivine and chromite: $r_{\text{chr}} = 0.02 \text{ cm}$, $r_{\text{opx}} = 0.3 \text{ cm}$, $\rho_{s_{\text{chr}}} = 4.6 \text{ g/cm}^3$, $\rho_{s_{\text{opx}}} = 3.3 \text{ g/cm}^3$, $\rho_l = 2.66 \text{ g/cm}^3$ and

Table 1 Average orthopyroxene composition of *N* microprobe and *n* LA-ICP-MS analyses, orthopyroxene in the section MG1-9 has not been analysed by LA-ICP-MS

	MG1-5			MG1-6			MG1-9			MG1-22		
	Core	Rim	Poik	Core	Rim	Poik	Core	Rim	Poik	Core	Rim	Poik
<i>N</i> (<i>n</i>)	15 (1)	26 (2)	30 (3)	11 (2)	22 (2)	46 (5)	7 (0)	9 (0)	19 (0)	10 (2)	17 (2)	17 (3)
SiO ₂	56.2	56.7	57.0	56.5	56.8	57.1	56.3	56.4	56.8	56.6	56.7	57.0
TiO ₂	0.10	0.11	0.11	0.11	0.11	0.11	0.09	0.11	0.11	0.08	0.09	0.09
Al ₂ O ₃	1.53	1.22	1.03	1.50	1.31	1.06	1.40	1.21	1.11	1.28	1.20	1.05
Cr ₂ O ₃	0.42	0.54	0.48	0.43	0.56	0.56	0.48	0.50	0.51	0.38	0.43	0.47
MgO	33.8	34.8	35.4	33.9	34.8	35.4	33.5	34.3	35.0	34.3	34.8	35.4
MnO	0.17	0.16	0.15	0.18	0.16	0.15	0.18	0.15	0.16	0.17	0.16	0.15
FeO	5.80	4.81	4.33	5.75	4.82	4.30	5.66	5.01	4.57	5.53	4.74	4.32
CaO	2.25	2.28	2.35	2.16	2.24	2.35	2.08	1.96	2.09	2.09	2.17	2.28
Na ₂ O	7.82	6.86	6.44	7.69	6.84	6.41	7.53	6.77	6.45	7.41	6.69	6.37
Total	0.77	0.61	0.44	0.94	0.69	0.50	1.35	0.86	0.69	0.67	0.67	0.47
Mg#	91.2	92.8	93.6	91.3	92.8	93.6	91.3	92.4	93.2	91.7	92.9	93.6
Sc	34	34	29	33	34	31				30	29	27
Ti	666	712	701	691	689	650				540	593	604
V	87	71	50	75	66	49				64	56	44
Cr	3324	2801	1994	3071	2704	2094				2458	2334	1725
Mn	1484	1359	1227	1491	1321	1214				1384	1268	1157
Co	63	49	38	62	48	38				51	41	32
Ni	607	577	530	575	569	530				565	526	479
Zn	44	37	31	40	33	27				35	30	26
Rb	bdl	bdl	bdl	bdl	bdl	bdl				bdl	bdl	bdl
Sr	0.93	0.26	0.10	0.29	0.21	0.09				0.24	0.39	0.28
Y	4.52	2.70	1.39	3.36	2.42	1.56				1.35	0.89	0.59
Zr	6.32	4.46	2.69	5.52	4.48	2.92				1.53	1.18	1.11
Nb	0.037	0.034	0.025	0.036	0.039	0.024				0.031	0.035	0.034
Ba	bdl	bdl	bdl	0.117	0.110	0.171				bdl	bdl	bdl
La	0.350	0.106	0.032	0.127	0.080	0.016				0.065	0.028	0.048
Ce	1.019	0.276	0.058	0.365	0.203	0.041				0.111	0.057	0.047
Pr	0.155	0.042	0.010	0.062	0.029	0.008				0.026	bdl	bdl
Nd	0.796	0.204	0.057	0.317	0.168	0.050				0.129	bdl	bdl
Sm	0.281	0.094	0.044	0.137	0.072	0.035				0.055	bdl	bdl
Eu	0.069	0.025	0.016	0.034	0.025	0.014				0.026	bdl	bdl
Gd	0.394	0.166	bdl	0.233	0.120	0.096				bdl	bdl	bdl
Tb	0.083	0.042	0.016	0.053	0.031	0.016				0.027	0.016	bdl
Dy	0.745	0.369	0.154	0.489	0.302	0.171				0.197	0.104	0.079
Ho	0.170	0.108	0.052	0.124	0.087	0.057				0.061	0.036	0.021
Er	0.600	0.398	0.230	0.467	0.350	0.246				0.241	0.179	0.121
Tm	0.098	0.075	0.048	0.078	0.071	0.050				0.050	0.040	0.027
Yb	0.701	0.616	0.413	0.658	0.553	0.450				0.424	0.341	0.247
Lu	0.114	0.108	0.083	0.104	0.097	0.082				0.072	0.067	0.054
Hf	0.180	0.181	0.117	0.202	0.181	0.130				0.063	0.051	0.063
Pb	0.099	0.070	0.057	0.166	0.107	0.108				0.378	0.144	0.232
U	0.058	0.021	0.010	0.022	0.013	0.002				0.027	0.012	0.014
Ce/Tb	12.327	6.642	3.542	6.831	6.448	2.546				4.140	3.644	

Main elements are given in wt%, trace elements in ppm

Core orthopyroxene oikocryst core zone, *rim* outermost ~ 100 μm of the core zones, *poik* poikilitic orthopyroxene, *bdl* below detection limit

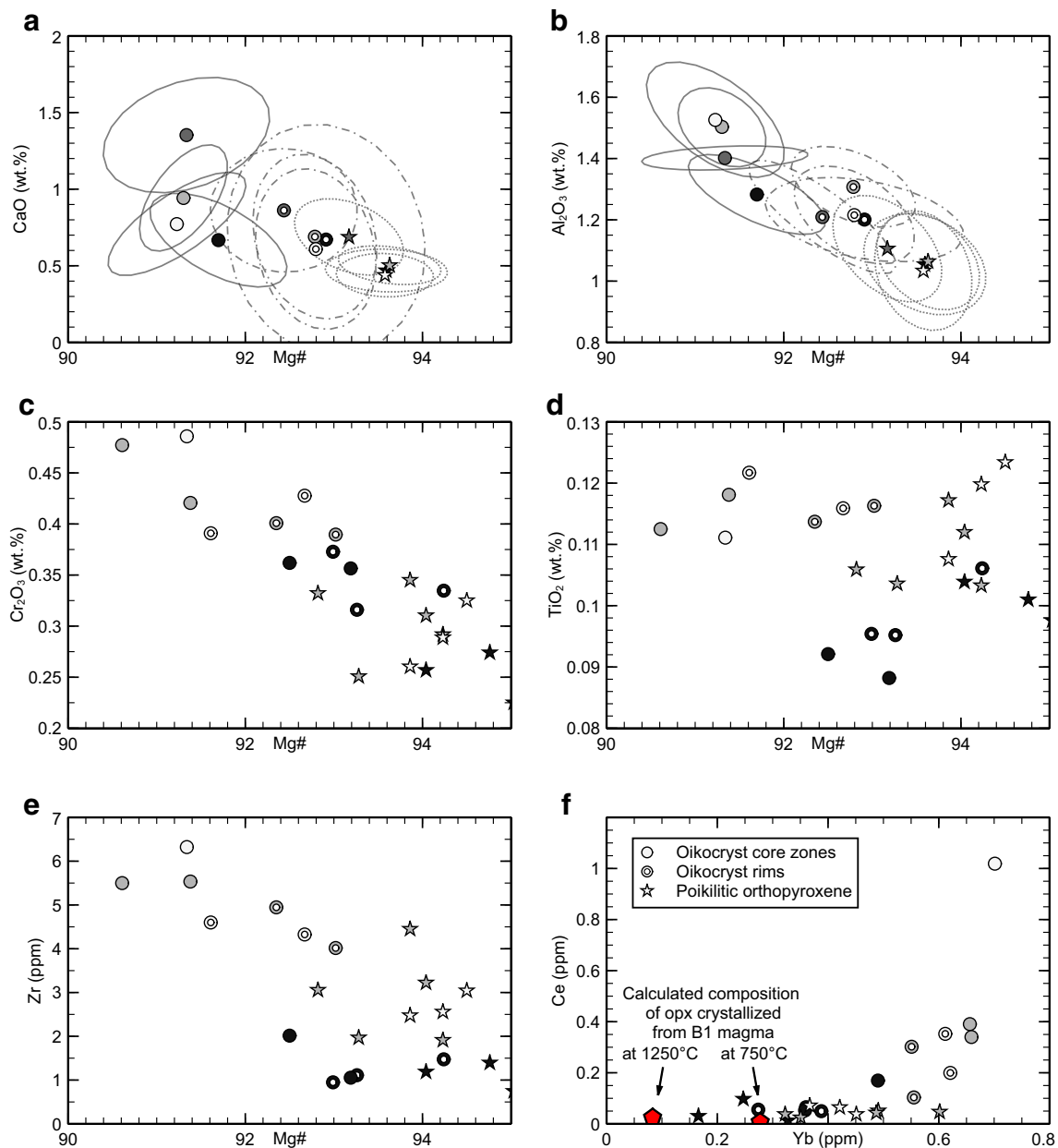


Fig. 7 Variations in orthopyroxene chemistry **a** CaO, **b** Al₂O₃, **c** Cr₂O₃, **d** TiO₂, **e** Zr concentrations versus Mg# and **f** Ce/Yb ratio. Data in **a** and **b** were collected by electron microprobe, and that in **c–f** by LA-ICP-MS. Different grey scales display different heights along

the MG1 (bright to dark from bottom to top). Filled circles represent orthopyroxene in oikocrysts core zones, open circles orthopyroxene along rims of oikocrysts core zones and stars poikilitic orthopyroxene. Ellipses indicate 66% confidence intervals for each data set

$\eta = 520$ g/cm s. Values for the density and viscosity of the liquid were calculated according to Bottinga and Weill (1970) and Shawn (1972), respectively for the B1 magma at 1150 °C. According to these values the settling velocity of olivine is ~ 75 times faster than that of the co-existing chromite (3.3×10^{-6} cm/s for chromite grains and 2.4×10^{-4} cm/s for olivine).

We have assumed that the chromite grains settled individually: the limited evidence for clusters with similar crystallographic orientations in the granular chromitite suggests that at least some of the chromite grains were joined on low-energy faces to form clusters with a correspondingly larger Stokes' settling velocity. However, clusters appear to be rare, and are generally small (Fig. 4a) and so we argue that cluster

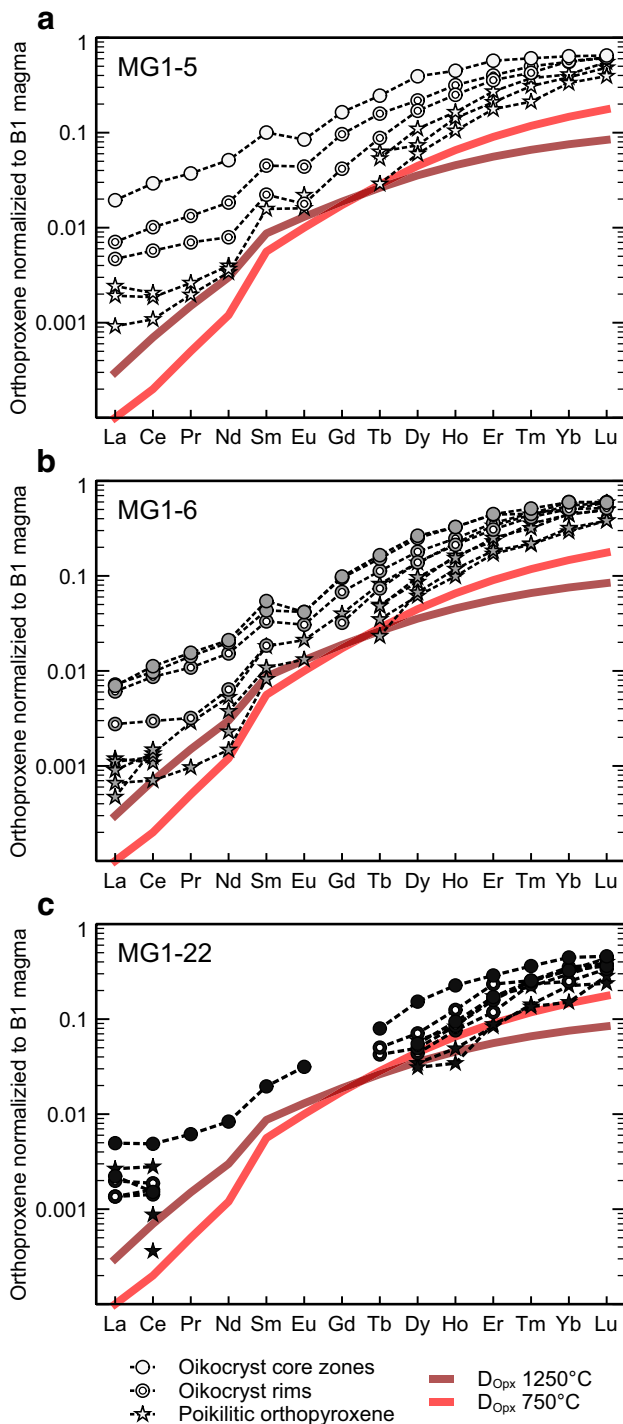


Fig. 8 REE concentrations of orthopyroxene along the MG1 sample profile (bottom to top), normalised to a postulated B1 magma (Barnes et al. 2010). Red lines depict calculated partition coefficients taken from Sun and Liang (2013) and Yao et al. (2012)

Table 2 Average olivine composition of *N* microprobe and *n* LA-ICP-MS analyses

	MG1-5	MG1-22
<i>N</i> (<i>n</i>)	5 (4)	9 (0)
SiO ₂	39.6	40.0
TiO ₂	bdl	bdl
Al ₂ O ₃	bdl	bdl
Cr ₂ O ₃	bdl	bdl
MgO	48.2	49.2
MnO	0.15	0.11
FeO	11.6	10.1
CaO	0.02	0.03
NiO	0.36	0.36
Total	99.9	99.8
Mg#	88.1	89.7
Sc	4	
Ti	14	
V	1	
Cr	21	
Mn	1205	
Co	144	
Ni	2810	
Zn	36	
Rb	bdl	
Sr	bdl	
Y	0.03	
Zr	0.05	
Nb	bdl	
Ba	bdl	
La	bdl	
Ce	bdl	
Pr	bdl	
Nd	bdl	
Sm	bdl	
Eu	bdl	
Gd	bdl	
Tb	bdl	
Dy	bdl	
Ho	bdl	
Er	bdl	
Tm	bdl	
Yb	0.0349	
Lu	0.0108	
Hf	0.0038	
Pb	bdl	
U	bdl	

Main elements are given in wt%, trace elements in ppm
bdl below detection limit

formation was not sufficient to significantly affect the relative settling rates of chromite and olivine.

We have also assumed settling from a static liquid. However, our conclusion that olivine and chromite have significantly different settling velocities is relevant even if the

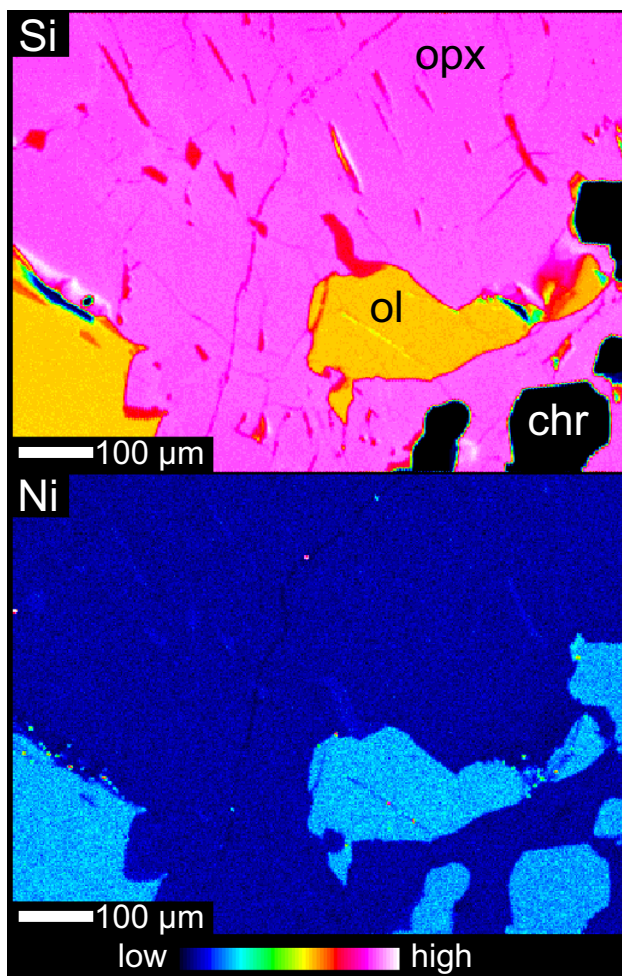


Fig. 9 Electron microprobe Si and Ni distribution map of orthopyroxene oikocrysts. The relative concentrations are indicated by the colour bar

magma were convecting. Martin and Nokes (1988, 1989) showed that crystal settling occurs in convecting magmas in which the convective velocity exceeds the settling velocity, when crystals enter the stagnant lower boundary layer. Settling from a convecting magma is slower than that from a static one, but in both situations larger denser crystals are more likely to settle faster than smaller lighter ones, to create a fining-upwards accumulation (Holness et al. 2017b). We note, however, that we did not detect such systematic changes in grain size.

While not arguing for accumulation of olivine primocrysts primarily by large-scale settling, we propose that the very different settling velocities support the hypothesis that the olivine primocrysts were introduced into the magma chamber by a crystal-bearing magma. A similar process was proposed by Barnes et al. (2016) to account for the oikocryst cores of the Ntaka Ultramafic Complex.

The second stage of our model is the peritectic replacement of the olivine primocrysts as a consequence of reaction with a more evolved (silica-rich) liquid in a solid–liquid reaction (e.g., Jackson 1961; Nicholson and Mathez 1991, 1995; Mathez et al. 1997; Meurer and Boudreau 1998a, b; Boorman et al. 2004; Barnes et al. 2016). The peritectic replacement of olivine primocrysts by orthopyroxene explains the observation that many cores have the same crystallographic orientation (i.e., several distinct olivine grains were replaced by a single orthopyroxene grain, attesting to a low nucleation rate for the replacive orthopyroxene, Fig. 5). It can also explain the negative Eu anomaly recorded by the oikocryst core zones, if the reactive liquid had already crystallised plagioclase. The high Mg# of the oikocryst core zones could be accounted for if the reactive liquid were evolved and oxidised, resulting in lower ferrous iron concentrations and the crystallisation of minerals with high Mg#.

The source of the infiltrating liquid is likely to have been the footwall pyroxenite (Fig. 11b). Upward flow may have been a consequence of gravitationally driven viscous compaction. There is no evidence for dislocation creep in these rocks, so any compaction must have occurred by a more cryptic process such as melt-assisted diffusion creep (Holness et al. 2017a). Alternatively, upwards flow could have been driven by a reduction in density caused by in situ fractionation.

The poikilitic aureoles grew after olivine replacement (Fig. 11c), and their composition suggests that they grew from a different, less evolved, liquid, suggesting that by this point any upward flow from the footwall had ceased. Critically, the composition of the poikilitic aureoles is consistent with growth from a non-fractionated B1 magma, suggesting that they grew in a highly porous and permeable mush from interstitial liquid in effective chemical communication with the bulk magma overlying the crystal mush.

Post-accumulation microstructural modification of the chromitite mush

The final stages of solidification involved textural modifications of the chromite grains that are not enclosed by oikocrysts (Fig. 11d). The microstructure of the granular chromitite is significantly different to that of the chromite enclosed by the oikocrysts (Figs. 3f, 6). It also has a different composition (Fig. 10). These features have been observed in many of the Bushveld chromitite layers (Cameron 1975; Hulbert and von Gruenewaldt 1985; Nicholson and Mathez 1991; Penberthy and Merkle 1999; Kottke-Levin et al. 2009; Voordouw et al. 2009; Junge et al. 2014). The reasons for these differences are not clear, but we suggest they may involve a combination of adcumulus growth, textural

Table 3 Average chromite composition of *N* microprobe analyses given in wt%

	MG1–5		MG1–6		MG1–9		MG1–22	
	Chromite in oikocrysts	Granular chromite	Chromite in oikocrysts	Granular chromite	Chromite in oikocrysts	Granular chromite	Chromite in oikocrysts	Granular chromite
<i>N</i>	40	37	40	27	21	31	19	25
TiO ₂	0.78	0.79	0.74	0.76	0.73	0.75	0.68	0.69
SiO ₂	0.05	0.01	0.04	0.00	0.03	0.01	0.03	0.02
Al ₂ O ₃	17.2	16.9	16.4	16.5	15.9	15.9	16.6	15.7
Cr ₂ O ₃	43.8	44.4	45.5	45.5	46.2	46.1	44.1	46.5
V ₂ O ₃	0.28	0.28	0.26	0.26	0.25	0.25	0.27	0.26
Fe ₂ O ₃	8.71	8.61	8.11	8.11	8.02	8.08	9.16	8.03
FeO	19.1	19.0	19.2	19.0	19.1	19.0	18.8	18.6
MnO	0.27	0.28	0.28	0.27	0.28	0.28	0.28	0.28
MgO	10.5	10.6	10.4	10.6	10.4	10.5	10.6	10.7
ZnO	0.06	0.05	0.06	0.06	0.05	0.05	0.05	0.05
NiO	0.16	0.16	0.14	0.14	0.15	0.15	0.16	0.13
Total	100.9	101.1	101.1	101.1	101.1	101.1	100.8	101.0
Mg#	49.6	49.7	49.1	49.8	49.4	49.6	50.1	50.7
Cr#	63.1	63.9	65.0	64.9	66.1	66.1	64.0	66.5

modification and diffusional modification of composition: the relative balance of these processes is not known.

If the chromitite formed by grain settling, the maximum packing of the chromite (and thus the maximum mode) would be that for close packing of spheres, or 74 vol%. More efficient packing can occur in accumulations with a range of grain sizes (Epstein and Young 1962; Jerram et al. 2003), but the narrow range of sizes observed for the grains enclosed by orthopyroxene means that we cannot call on the effect of a strongly polydisperse grain population to increase the packing efficiency. Moreover, settling will result in a disordered grain arrangement. Random loose packing of single grains (defined as the loosest, mechanically stable packing state) results in 56–54 vol% solids (Onoda and Liniger 1990; Ciamarra and Coniglio 2008; Zamponi 2008; Farrell et al. 2010), and this packing can be reduced even further if grains settled as clusters (Heaney et al. 1995; Dong et al. 2006; Yang et al. 2007).

The evidence shown in Fig. 4 is supportive of the formation of at least some clusters of chromite grains. Clusters or chain formation by auto-nucleation or synneusis generally results in grains being joined by low-energy grain boundaries, resulting in a crystallographic relationship between the individual grains. Prichard et al. (2015) argue that inter-grain relationships within nodular chromite, in which grains in the central region share the same $\langle 110 \rangle$ axis as grains in the outer parts of the nodule indicate self-nucleation (of the outer grains on the inner grains). Such relationships are not evident in the MG1 chromitite. While some chromite grains share a {100} contact face (Fig. 4d, cluster 1), most of the clusters we examined share a common axis (Fig. 4d, e), but with no preference for any particular common axis (see the

percentages for each axis given at the bottom of Fig. 4): these features are most likely a result of cluster formation by synneusis. However, there are only few clusters in evidence in Fig. 4 and we argue that most of the chromite in the MG1 chromitite accumulated as single grains.

The chromite mode in the poikilitic orthopyroxene aureoles is 50–60 vol%. This is in the range expected for a random loose packing of single monodisperse grains, and suggests that the spatial distribution and grain size population of chromite grains in the earliest stages of mush formation was preserved by early enclosure by the orthopyroxene. However, the almost 100 vol% chromite mode in the granular chromitites demonstrates that they must have experienced some adcumulus growth.

Adcumulus growth of chromite grains in close proximity to interstitial orthopyroxene would necessitate the localised suppression of orthopyroxene nucleation and growth. The replacement of adjacent olivine primocrysts by single grains of orthopyroxene and the continued growth of the orthopyroxene grains into the chromite mush to form extended oikocrysts is certainly consistent with this. One possible mechanism to create the observed microstructure is therefore to have the interstitial liquid crystallising both chromite and orthopyroxene, with inhibition of orthopyroxene nucleation confining orthopyroxene growth to the immediate neighbourhood of olivine primocrysts. Adcumulus overgrowth of the chromite near the magma-mush interface would then have resulted in the densification of the chromite mush. The complete absence of plagioclase in the MG1 chromitite is consistent with this hypothesis. The last stages of solidification involved the crystallisation of a highly evolved, hydrous liquid to form the small amounts of biotite and hornblende.

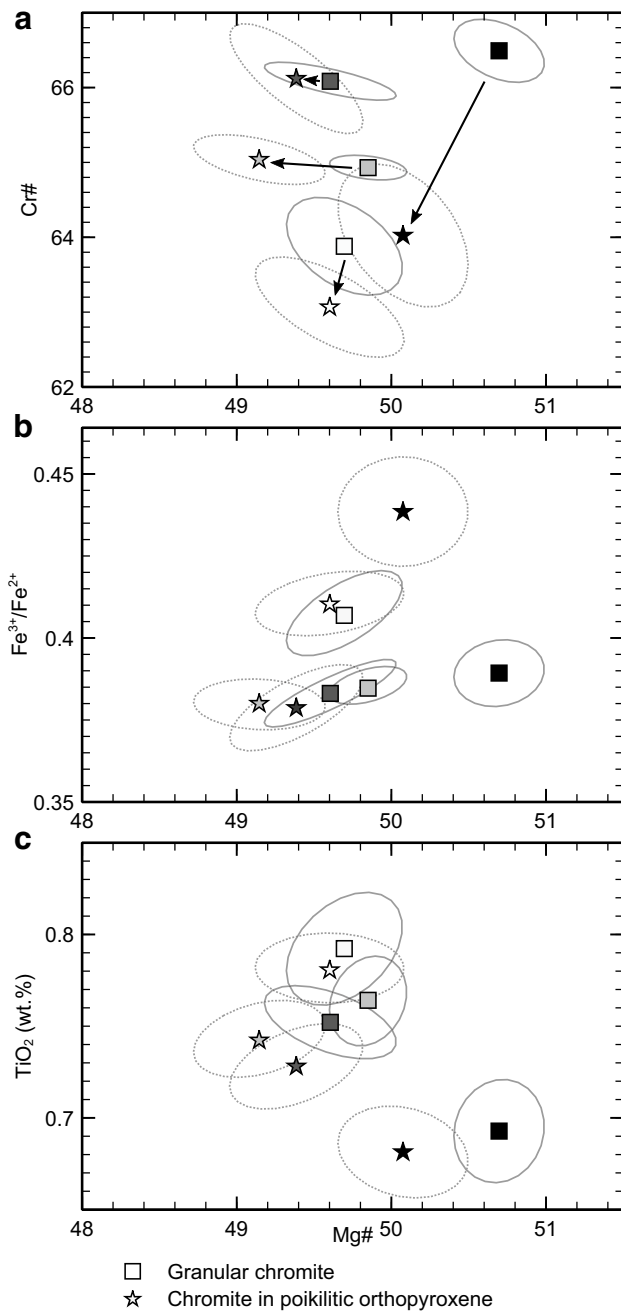


Fig. 10 Variations in chromite chemistry. **a** Cr#, **b** Fe³⁺/Fe²⁺ and **c** TiO₂ concentrations versus Mg# collected by electron microprobe. Different grey scales display different heights along the MG1 (bright to dark from bottom to top). Ellipses indicate 66% confidence intervals for each data set

The coarser grain size and granular microstructure of the chromite adcumulate would then be a simple consequence of its essentially monomineralic composition, permitting rapid grain boundary migration and the attainment of textural equilibrium, driven by the minimisation of interfacial energies (e.g., Hunter 1987, 1996; Holness and Vernon

2015). Textural equilibration resulted in the smoothing of grain boundaries, the attainment of 120° triple junctions and the onset of normal grain growth driven by differences in grain boundary curvature (Thomson 1887; Bulau et al. 1979; Holness 2005, 2007). CSD data (Fig. 6) reveal a rotation consistent with normal grain growth, with a reduction in smaller grains and increase in larger grains in the granular chromitite compared to the population of grains enclosed in the orthopyroxene. The difference in composition between the granular chromitite and the chromite enclosed by oikocrysts (Fig. 10) could then be accounted for as the chromite enclosed by orthopyroxene would have equilibrated with the surrounding pyroxene, whereas the granular chromitite retained its original composition.

Implications for chromitite formation models

The focus of this paper has been on the oikocrysts within the chromitite, but our textural and chemical observations can also be used to shed some light on the formation of the chromitite layers themselves. Numerous models and ideas have been proposed to account for the formation of chromitite layers in layered intrusions (see Maier et al. 2013; Cawthorn 2015 for comprehensive recent reviews), including those based on the mobilisation of cumulate slurries (Maier et al. 2013). Importantly, we see no fining-upwards of the size in chromite grains enclosed in the oikocrysts (i.e., those most likely to retain their original size), suggesting that the slurry model cannot account for these particular chromitite layers.

Conclusions

Orthopyroxene oikocrysts in the MG1 chromitite layer of the Western Bushveld Complex grew during a complex series of steps, involving the peritectic replacement of cumulus olivine triggered by an upwards percolating, incompatible element enriched, evolved melt. The core zones were then overgrown by poikilitic orthopyroxene in equilibrium with the parental melt B1 near the magma-crystal mush interface. Finally, post-cumulus adcumulus chromite growth followed by annealing of chromite crystals outside the oikocrysts led to the formation of granular chromitite.

Our integrated approach provides an understanding of different magmatic processes, controlling both the geochemical and the textural evolution of oikocrysts. Although this study describes small-scale phenomena, similar oikocrysts are observed in other parts of the Bushveld Complex, suggesting that the history we have outlined here may be common in layered mafic intrusions.

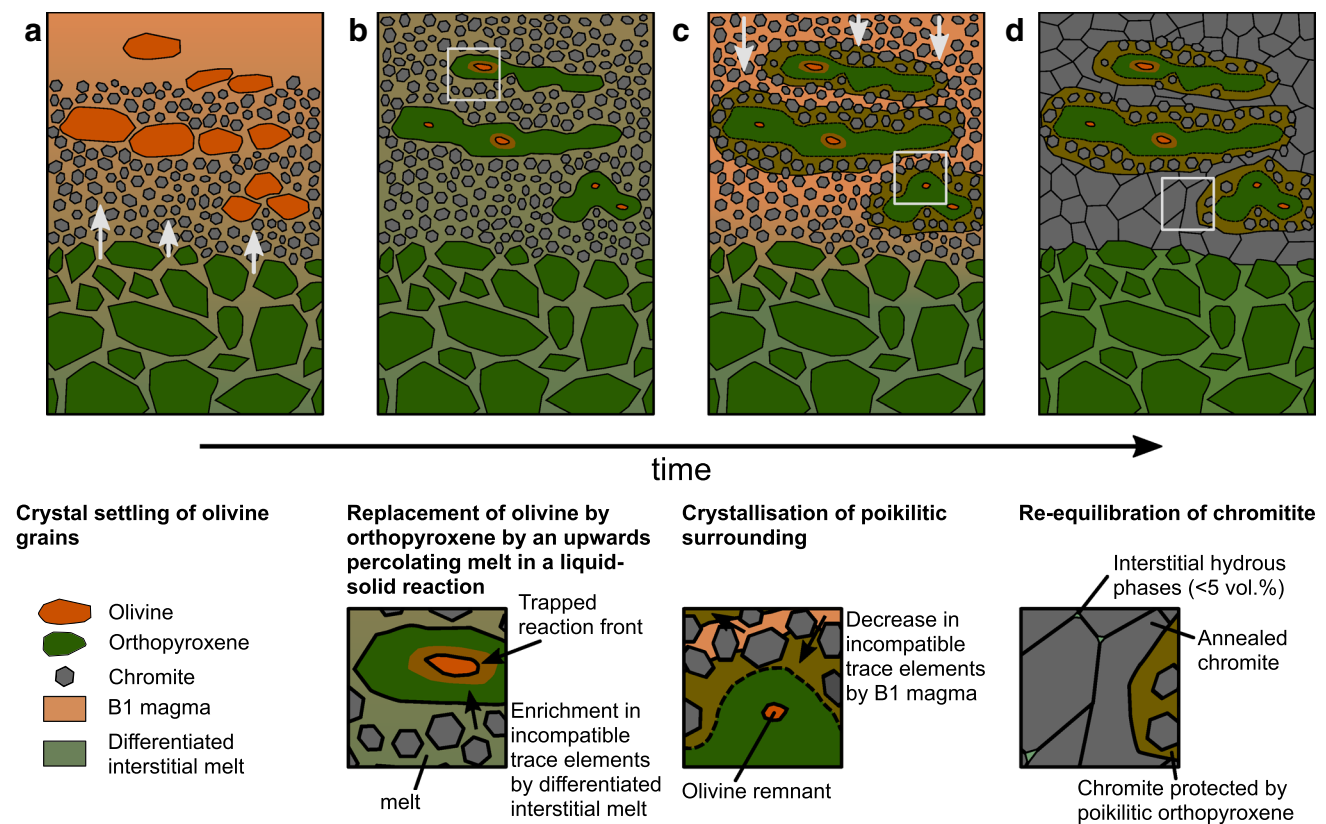


Fig. 11 Proposed model for the formation of orthopyroxene oikocrysts in the MG1 chromitite layer. See text for further explanation

Acknowledgements FEDK was supported by the German Federal Ministry of Education and Research (BMBF), Grant FKZ 033R119C, ZV by Marie Skłodowska-Curie Individual European Fellow grant. Cronimet Chrome Mining SA (Pty) Ltd. is thanked for provision of drill core material. We are grateful to M. Oeser-Rabe and S. Schuth for help with the LA-ICP-MS analyses, also assistance by K. Born and P. Czaja at the SEM and microprobe at the Museum für Naturkunde Berlin are greatly acknowledged. Fruitful discussions with M. C. Hoffmann and I. V. Veksler were highly appreciated. Helpful reviews by two anonymous reviewers and editor Chris Ballhaus greatly improved the original paper.

References

- Albrecht M, Derrey IT, Horn I, Schuth S, Weyer S (2014) Quantification of trace element contents in frozen fluid inclusions by UVfs-LA-ICP-MS analysis. *J Anal Atom Spectrom* 29:1034–1041
- Barnes SJ (1986) The effect of trapped liquid crystallization on cumulus mineral compositions in layered intrusions. *Contrib Miner Petrol* 93:524–531
- Barnes SJ, Maier WD, Curl EA (2010) Composition of the marginal rocks and sills of the Rustenburg layered suite, Bushveld complex, South Africa: implications for the formation of the platinum-group element deposits. *Econ Geol* 105:1491–1511
- Barnes SJ, Mole DR, Le Vaillant M, Campbell MJ, Verral, Roberts MP, Evans NJ (2016) Poikilitic textures, heteradcumulates and zoned orthopyroxenes in the ntaka ultramafic complex, Tanzania: implications for crystallization mechanisms of oikocrysts. *J Petrol* 57:1171–1198
- Boorman S, Boudreau AE, Kruger FJ (2004) The lower zone-critical zone transition of the bushveld complex: a quantitative textural study. *J Petrol* 45:1209–1235
- Bottinga Y, Weill DF (1970) Densities of liquid silicate systems calculated from partial molar volumes of oxide components. *Am J Sci* 269
- Bulau JR, Waff HS, Tyburczy JA (1979) Mechanical and thermodynamic constraints on fluid distribution in partial melts. *J Geophys Res B Solid Earth* 84:6102–6108
- Cameron EN (1969) Postcumulus changes in the eastern Bushveld complex. *Am Mineral* 54:754–779
- Cameron EN (1975) Postcumulus and subsolidus equilibration of chromite and coexisting silicates in the eastern Bushveld Complex. *Geochim Cosmochim Acta* 39:1021–1033
- Cameron EN (1977) Chromite in the central sector of the eastern Bushveld Complex, South Africa. *Am Mineral* 62:1082–1096
- Cameron EN (1980) Evolution of the lower critical zone, central sector, eastern Bushveld Complex, and its chromite deposits. *Econ Geol* 75:845–871
- Campbell IH (1968) The origin of heteradcumulate and adcumulate textures in the Jimberlana Norite. *Geol Mag* 105:378–383
- Campbell IH (1987) Distribution of orthocumulate textures in the Jimberlana intrusion. *J Geol* 95:35–53

- Cawthorn RG (2015) The Bushveld complex, South Africa. In: Charlier B, Namur O, Latypov R, Tegner C (eds) Layered intrusions. Springer, Dordrecht, pp 517–587
- Ciamarra MP, Coniglio A (2008) Random very loose packings. *Phys Rev Lett* 101:128001
- Collinet M, Charlier B, Namur O, Oeser M, Médard E, Weyer S (2017) Crystallization history of enriched shergottites from Fe and Mg isotope fractionation in olivine megacrysts. *Geochim Cosmochim Acta* 207:277–2997
- Dong KJ, Yang RY, Zou RP, Yu AB (2006) Role of interparticle forces in the formation of random loose packing. *Phys Rev Lett* 96:145505
- Eales HV, Cawthorn RG (1996) The Bushveld complex. In: Cawthorn RG (ed) Layered intrusions. Elsevier, Oxford, pp 181–229
- Eales HV, de Klerk WJ, Teigler B (1990) Evidence for magma mixing processes within the critical and lower zones of the northwestern Bushveld complex, South Africa. *Chem Geol* 88:261–278
- Eales HV, Teigler B, Maier WD (1993) Cryptic variations of minor elements Al, Cr, and Mn in lower and critical zone orthopyroxenes of the Western Bushveld complex. *Miner Mag* 57:257–264
- Epstein N, Young MJ (1962) Random loose packing of binary mixtures of spheres. *Nature* 196:885–886
- Farrell GR, Martini KM, Menon N (2010) Loose packings of frictional spheres. *Soft Matter* 6:2925–2930
- Godel B, Barnes S-J, Maier WD (2011) Parental magma composition inferred from trace element in cumulus and intercumulus silicate minerals: an example from the lower and lower critical zones of the Bushveld complex, South-Africa. *Lithos* 125:537–552
- Guillong M, Meier D, Allan MM, Heinrich CA, Yardley BWD (2008) SILLs: a MATLAB-based program for the reduction of laser ablation ICP-MS data of homogeneous materials and inclusions. *Mineral Assoc Can Short Course* 40:328–333
- Harmer RE, Sharpe MR (1985) Field relations and strontium isotope systematics of the marginal rocks of the eastern Bushveld complex. *Econ Geol* 80:813–837
- Heaney DF, German RM, Ahn IS (1995) The gravitational effects on low solid-volume fraction liquid-phase sintering. *J Mater Sci* 30:5808–5812
- Higgins MD (2000) Measurement of crystal size distributions. *Am Mineral* 85:1105–1116
- Holness MB (2005) Spatial constraints on magma chamber replenishment events from textural observations of cumulates: the rum layered intrusion, Scotland. *J Petrol* 46:1585–1601
- Holness MB (2007) Textural immaturity of cumulates as an indicator of magma chamber processes: infiltration and crystal accumulation in the Rum Eastern layered intrusion. *J Geol Soc* 164:529–539
- Holness MB, Vernon RH (2015) The influence of interfacial energies on igneous microstructures. In: Charlier B, Namur O, Latypov R, Tegner C (eds) Layered intrusions. Springer, Dordrecht, pp 183–228
- Holness MB, Vukmanovic Z, Mariani E (2017a) Assessing the role of compaction in the formation of adcumulates: a microstructural perspective. *J Petrol* 58:643–673
- Holness MB, Farr R, Neufeld JA (2017b) Crystal settling and convection in the Shiant Isles Main Sill. *Contrib Miner Petrol* 172:1–25
- Hulbert LJ, von Gruenewaldt G (1985) Textural and compositional features of chromite in the lower and critical zones of the Bushveld complex South of Potgietersrus. *Econ Geol* 80:872–893
- Hunter RH (1987) Textural equilibrium in layered igneous rocks. In: Parson I (ed) Origins of igneous layering. Springer, Dordrecht
- Hunter RH (1996) Texture development in cumulate rocks. In: Cawthorn RG (ed) Layered intrusions. Elsevier, Oxford, pp 77–101
- Ivanic TJ, Nebel O, Jourdan F, Faure K, Kirkland CL, Belousova EA (2015) Heterogeneously hydrated mantle beneath the late Archean Yilgarn Craton. *Lithos* 238:76–85
- Jackson ED (1961) Primary textures and mineral associations in the ultramafic zone of the Stillwater Complex, Montana. *US Geol Surv Prof Pap* 358
- Jarosewich E, Nelen JA, Norberg JA (1980) Reference samples for electron microprobe analysis. *Geostand Geoanal Res* 4:43–47
- Jerram DA, Cheadle MC, Philpotts AR (2003) Quantifying the building blocks of igneous rocks: are clustered crystal frameworks the foundation? *J Petrol* 44:2033–2051
- Junge M, Oberthuer T, Melcher F (2014) Cryptic variation of chromite chemistry, platinum group element and platinum group mineral distribution in the UG-2 chromitite: an example from the Karee Mine, western Bushveld complex, South Africa. *Econ Geol* 109:795–810
- Junge M, Oberthuer T, Osbahr I, Gutter P (2016) Platinum-group elements and minerals in the lower and middle group chromitites of the western Bushveld Complex, South Africa. *Miner Depos* 51:841–852
- Kotke-Levin J, Tredoux M, Graebe PJ (2009) An investigation of the geochemistry of the Middle Group of the eastern Bushveld complex, South Africa Part 1—the chromitite layers. *Appl Earth Sci* 118:111–130
- Lazarov M, Horn I (2015) Matrix and energy effects during in-situ determination of Cu isotope ratios by ultraviolet-femtosecond laser ablation multicollector inductively coupled plasma mass spectrometry. *Spectrochim Acta Part B Atom Spectrosc* 111:64–73
- Lee CA, Parry SJ (1988) Platinum-group element geochemistry of the lower and middle group chromitites of the eastern Bushveld complex. *Econ Geol* 83:1127–1139
- Maier WD (1995) Olivine oikocrysts in Bushveld Anorthosite; some implications for cumulate formation. *Can Mineral* 33:1011–1022
- Maier WD, Barnes S-J, Groves DI (2013) The Bushveld Complex, South Africa: formation of platinum–palladium, chrome- and vanadium-rich layers via hydrodynamic sorting of a mobilized cumulate slurry in a large, relatively slowly cooling, subsiding magma chamber. *Miner Depos* 48:1–56
- Martin D, Nokes R (1988) Crystal settling in a vigorously converting magma chamber. *Nature* 332:534–536
- Martin D, Nokes R (1989) A fluid-dynamical study of crystal settling in convecting magmas. *J Petrol* 30:1471–1500
- Mathez EA (1995) Magmatic metasomatism and formation of the Merensky Reef, Bushveld complex. *Contrib Miner Petrol* 119:277–286
- Mathez EA, Hunter RH, Kinzler R (1997) Petrologic evolution of partially molten cumulate: the Atok section of the Bushveld complex. *Contrib Miner Petrol* 129:20–34
- Mathison CI (1987) Pyroxene oikocrysts in troctolitic cumulates-evidence for supercooled crystallisation and postcumulus modification. *Contrib Miner Petrol* 97:228–236
- Merkle RKW (1992) Platinum-group minerals in the middle group of chromitite layers at Marikana, western Bushveld complex: indications for collection mechanisms and postmagmatic modification. *Can J Earth Sci* 29:209–221
- Meurer WP, Boudreau AE (1998a) Compaction of igneous cumulates Part I: geochemical consequences for cumulates and liquid fractionation trends. *J Geol* 106:281–292
- Meurer WP, Boudreau AE (1998b) Compaction of igneous cumulates Part II: compaction and the development of igneous foliations. *J Geol* 106:293–304
- Meurer WP, Claeson DT (2002) Magma replenishment, and the significance of poikilitic textures, in the lower main zone of the western Bushveld complex, South Africa. *J Petrol* 43:607–629
- Naldrett AJ, Wilson AH, Kinnaird J, Chunnett G (2009) PGE tenor and metal ratios within and below the Merensky Reef, Bushveld complex: implications for its genesis. *J Petrol* 50:625–659

- Namur O, Abily B, Boudreau AE, Blanchette F, Bush JWM, Ceuleneer G, Charlier B, Donaldson CH, Duchesne JC, Higgins MD, Morata D, Nielsen TFD, O'Driscoll B, Pang KN, Peacock T, Spandler C, Toramaru A, Vekler IV (2015) Igneous layering in basaltic magma chambers. In: Charlier B, Namur O, Latypov R, Tegner C (eds) Layered intrusions. Springer, Dordrecht, pp 75–152
- Nicholson DM, Mathez EA (1991) Petrogenesis of the Merensky Reef in the Rustenburg section of the Bushveld complex. *Contrib Miner Petrol* 107:293–309
- O'Driscoll B, Donaldson CH, Troll VR, Jerram DA, Emeleus CH (2007) An origin for harrisitic and granular olivine in the Rum Layered Suite, NW Scotland: a crystal size distribution study. *J Petrol* 48:253–270
- O'Driscoll B, Donaldson CH, Daly JS, Emeleus CH (2009) The roles of melt infiltration and cumulate assimilation in the formation of anorthosite and a Cr-spinel seam in the Rum Eastern Layered Intrusion, NW Scotland. *Lithos* 111:6–20
- Oberthuer T, Junge M, Rudashevsky N, de Meyer E, Gutter P (2016) Platinum-group minerals in the LG and MG chromitites of the eastern Bushveld complex, South Africa. *Miner Depos* 51:71–87
- Oeser M, Weyer S, Horn I, Schuth S (2014) High-precision Fe and Mg isotope ratios of silicate reference. *Geostand Geoanal Res* 38:311–328
- Onoda GY, Liniger EG (1990) Random loose packings of uniform spheres and the dilatancy onset. *Phys Rev Lett* 64:2727–2730
- Penberthy CJ, Merkle RKW (1999) Lateral variations in the platinum-group element content and mineralogy of the UG2 Chromitite Layer, Bushveld complex. *S Afr J Geol* 102:240–250
- Prichard HM, Barnes SJ, Godel B, Reddy SM, Vukmanovic Z, Halfpenny A, Neary CR, Fisher PC (2015) The structure of and origin of nodular chromite from the Troodos ophiolite, Cyprus, revealed using high-resolution X-ray computed tomography and electron backscatter diffraction. *Lithos* 218–219:87–98
- Scoates JS, Friedman RM (2008) Precise age of the platiniferous Merensky Reef, Bushveld complex, South Africa, by the U-Pb zircon chemical abrasion ID-TIMS technique. *Econ Geol* 103:465–471
- Scoates JS, Wall CJ (2015) Geochronology of layered intrusions. In: Charlier B, Namur O, Latypov R, Tegner C (eds) Layered intrusions. Springer, Dordrecht, pp 3–74
- Scoon RN, Teigler B (1994) Platinum-group element mineralization in the critical zone of the western Bushveld complex; I, Sulfide poor-chromitites below the UG-2. *Econ Geol* 89:1094–1121
- Shawn HR (1972) Viscosities of magmatic silicate liquids; an empirical method of prediction. *Am J Sci* 272:870–893
- South African Committee for Stratigraphy (ed) (1980) Stratigraphy of Southern Africa. Part 1. Lithostratigraphy of South Africa, South West Africa/Namibia, and the Republics of Boputhatswana, Transkei, and Venda. Geological Survey of South Africa
- Sun C, Liang Y (2013) Distribution of REE and HFSE between low-Ca pyroxene and lunar picritic melts around multiple saturation points. *Geochim Cosmochim Acta* 119:340–358
- Tegner C, Wilson JR (1995) Textures in a poikilitic olivine gabbro cumulate: evidence for supercooling. *Miner Petrol* 54:161–173
- Teigler B (1990) Platinum group element distribution in the lower and middle group chromitites in the western Bushveld complex. *Miner Petrol* 42:165–179
- Thomson W (1887) On the division of space with minimum partitional area. *Acta Math* 11:121–134
- Ulmer GC, Gold DP (1982) Monomineralicity and oikocrysts: keys to cumulus cooling rates? In: Magmatic processes of early planetary crusts: magma oceans and stratiform layered intrusions
- Vekler IV, Reid DL, Dulski P, Keiding JK, Schannor M, Hecht L, Trumbull RB (2015) Electrochemical processes in a crystal mush: cyclic units in the upper critical zone of the Bushveld complex, South Africa. *J Petrol* 56:1229–1250
- Vernon RH (2004) A practical guide to rock microstructure. Cambridge University Press, Cambridge
- Voordouw R, Gutzmer J, Beukes NJ (2009) Intrusive origin for Upper Group (UG1, UG2) stratiform chromitite seams in the Dwars River area, Bushveld complex, South Africa. *Miner Petrol* 97:75–94
- Wager LR (1961) A note on the origin of ophitic texture in the chilled olivine gabbro of the Skaergaard intrusion. *Geol Mag* 98:353–364
- Wager LR, Brown GM, Wadsorth WJ (1960) Types of igneous cumulates. *J Petrol* 1:73–85
- Wilson AH (2012) A chill sequence to the Bushveld complex: insight into the first stage of emplacement and implications for the parental magmas. *J Petrol* 53:1123–1168
- Yang RY, Zou RP, Dong KJ, An XZ, Yu A (2007) Simulation of the packing of cohesive particles. *Comput Phys Commun* 177:206–209
- Yao L, Sun C, Liang Y (2012) A parameterized model for REE distribution between low-Ca pyroxene and basaltic melts with applications to REE partitioning in low-Ca pyroxene along a mantle adiabat and during pyroxenite-derived melt and peridotite interaction. *Contrib Miner Petrol* 164:261–280
- Zamponi F (2008) Mathematical physics: packings close and loose. *Nature* 453:606–607